Inorganic Chemistry

pubs.acs.org/IC

Communication

Creating High-Number Defect Sites through a Bimetal Approach in Metal−Organic Frameworks for Boosting Trace SO_2 Removal

Hui Ping Zhang, Qing Yun Zhang, Xue Feng Feng,* Rajamani Krishna, and Feng Luo*

Cite This: *Inorg. Chem.* 2022, 61, 16986−16991

Read Online

ACCESS | Metrics & More | Article Recommendations | Supporting Information

ABSTRACT: Herein, we represent a bimetallic approach to enhance the defect number, leading to eight defect sites per node in a metal−organic framework, showing both a higher SO_2 adsorption capacity and higher SO_2/CO_2 selectivity. The results can be further strongly supported by density functional theory calculations.

Defective metal−organic frameworks (MOFs), representing a unique and significant branch of MOF science, are now receiving tremendous attention.[1−7] This proven matter is often viewed to possess a unique advantage in pore generation and host−guest interactions for many advanced applications in catalysis, adsorption, separation, and so on, relative to the nondefective MOFs.[8−30] Thereby, there has been great concern on the creation of high-number defective MOFs, in view of the relationship between defective sites and active sites. However, there still remains a crucial restriction, viz. a trade-off between the number of defect sites and the stability of MOFs, where a high number of defect sites commonly causes a decrease in the stability of MOFs and even leads to the collapse of MOFs.[31,32] Until now, MOFs showing a high number of defect sites per node are still scarce, especially for numbers of defect sites greater than six.[33]

UiO-66, built on the well-known second building blocks of the $Zr_6O_4(OH)_4$ node, represents one of the most stable MOFs.[34−36] Generally, UiO-66 is a nondefective MOF with 12 linkers per $Zr_6O_4(OH)_4$ node. However, if we change the synthesis conditions by adding a large excess of monocarboxylic acid as a modulation, then we can obtain defective UiO-66 (Scheme 1).[37−39] For example, formic acid, a simple but effective modulation, was often chosen in the literature,[37−39] and the mode in the resulting defect size stems from the replacement of terephthalate linkers by some nonlinker formate. As a result, as shown in Scheme 1, when two terephthalate linkers are replaced by two nonlinker formates, then this will generate two defect sites per $Zr_6O_4(OH)_4$ node, while, accordingly, a four-replacement could output four defect sites per $Zr_6O_4(OH)_4$ node. However, it is also synthetically difficult to create a high number of defect sites of more than four per $Zr_6O_4(OH)_4$ node, mainly restricted by the trade-off between the stability of MOFs and the number of defect sites. In other cases, Atzori et al. demonstrated the use of benzoic acid as a modulator to create a maximum defect number of 4.4 per node.[40] Voort et al. employed a hemilabile linker of 4-sulfonatobenzoate as a modulator to enhance the maximum defect number up to 6 per node.[33] However, defect numbers bigger than 6 per $Zr_6O_4(OH)_4$ or analogues have not been observed until now.

Scheme 1. Comparison of Nondefective UiO-66, Defective UiO-66, and Our Defective MOF MOF-Th-Co-66

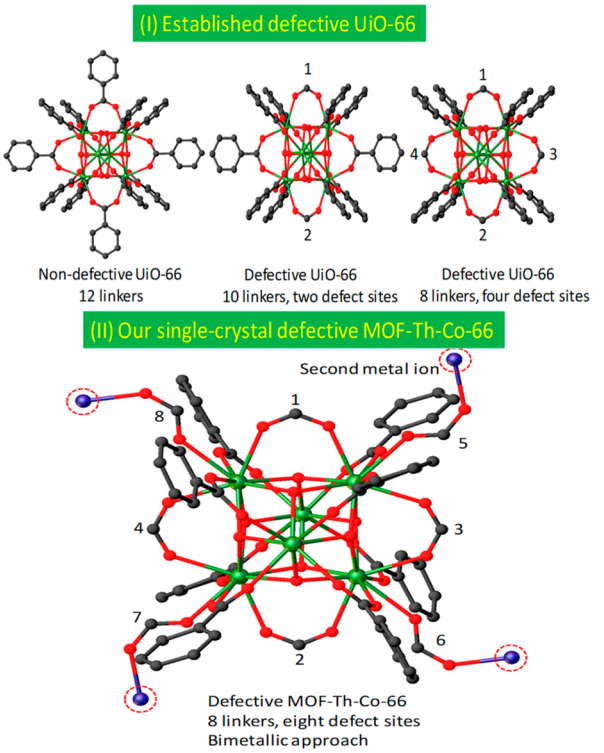

In defect science, how to structurally disclose the defect site represents another important issue.[34−36] Some other solutions have been developed. For example, a combined characterization composed of NMR (nuclear magnetic resonance), IR

Received: September 7, 2022
Published: October 20, 2022

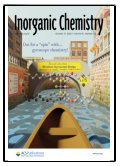

https://doi.org/10.1021/acs.inorgchem.2c03177
Inorg. Chem. 2022, 61, 16986−16991

(infrared spectrum), and TGA (thermogravimetry analysis) represents the commonly used method in the literature.[33−40] However, this just reflects an average defect concentration within an MOF, rather than detailed structure information on defect sites per cluster. Recent advances disclosed that local defect arrangement can be resolved by spatially resolved techniques such as confocal fluorescence microscopy,[41] fluorescence lifetime imaging,[42] and atomic force microscopy[43] but is still restricted in the limited spatial resolution of ca. 200 nm. Very recently, this can be further improved to a spatial resolution of ca. 5 nm via scanning electron diffraction (SED).[44] However, these technologies are still some distance from the atomic resolution level.

In this work, we report the structure, characterization, and application of a single-crystal defective MOF, namely, **MOF-Th-Co-66**, through a bimetallic approach (Scheme 1), which contains a $Th_6O_4(OH)_4$ cluster, similar to the well-known $Zr_6O_4(OH)_4$ cluster in UiO-66.

The synthesis of **MOF-Th-Co-66** is shown in the Supporting Information, and the phase purity was confirmed by powder X-ray diffraction (Figure S1). The structure was determined by single-crystal X-ray diffraction, given in the tetragonal system with the *I4/m* space group. The basic building unit is the $Th_6O_4(OH)_4$ cluster, which shows high comparability with the $Zr_6O_4(OH)_4$ cluster in UiO-66 (Figure 1a). The combination of $Th_6O_4(OH)_4$ clusters, Co(II) ions,

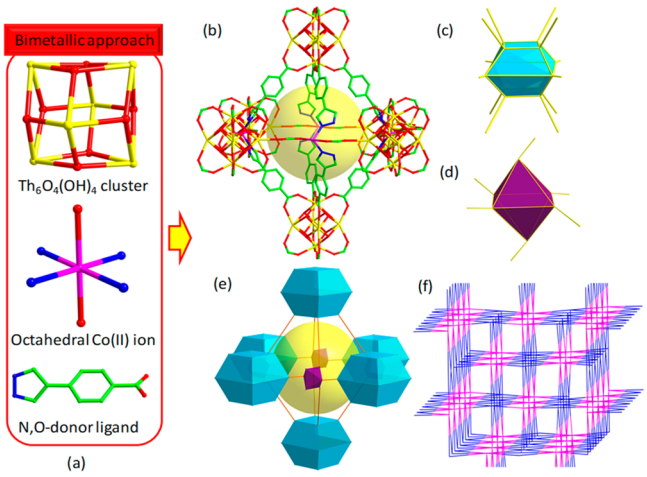

Figure 1. (a) Bimetallic approach based on $Th_6O_4(OH)_4$ cluster, octahedral Co(II) ions, and N,O-donor ligands. (b) View of $Th_{36}Co_4$ octahedral cage. (c) View of $Th_6O_4(OH)_4$ cluster. (d) View of single Co(II) ion. (e) Topological view of $Th_{36}Co_4$ octahedral cage. (f) Topological view of (6,12)-connected net.

and N,O-donor ligands of L^{2-} [H_2L = 4-(1*H*-pyrazol- 4-yl)benzoic acid] creates a $Th_{36}Co_4$ octahedral cage with an aperture of ca. 0.9 nm (Figure 1b). Topology analysis discloses the $Th_6O_4(OH)_4$ cluster as a 12-connecting node in a highly rare convex decahedron configuration and the Co(II) ion as a 6-connecting node in a common octahedral configuration, resulting in the overall (6,12)-connecting net with the $(4^{13}6^2)(4^{44}6^{22})$ topology symbol (Figure 1c−f).[45,46] A topological description of the $Th_{36}Co_4$ octahedral cage and the (6,12)-connected net is shown in Figure 1e,f, respectively.

In **MOF-Th-Co-66**, the $Th_6O_4(OH)_4$ clusters are not linked directly through L^{2-} linkers. This connecting mode is very different from $Zr_6O_4(OH)_4$ in UiO-66, where $Zr_6O_4(OH)_4$ clusters are directly bridged by organic linkers. A comparison of connectivity between them is shown in Figure S2. The difference can be well explained by the soft and hard acid base theory. The $Zr_6O_4(OH)_4$ cluster favors O-donor ligands, while the N-donor ligand is more favorable for Co(II) ions. Thus, the N,O-donor ligands of L^{2-} act as a good bridge between $Th_6O_4(OH)_4$ clusters and Co(II) ions in **MOF-Th-Co-66**. In addition, each $Th_6O_4(OH)_4$ cluster in **MOF-Th-Co-66** also contains eight formate modulators (Scheme 1) with four being nonlinkers (commonly encountered defect site in UiO-66) and the other four being linkers (potential defect site that was not observed in the literature). The coordination mode for these formate modulators is the bidentate mode, but displaying two distinct configurations such as *syn*−*syn* for nonlinkers and *anti*−*syn* for linkers. This situation is very different from that observed in defective UiO-66, where just nonlinkers of the formate modulator were observed (Scheme 1). Generally speaking, the 12-linker in UiO-66 is viewed to give a complete occupation on the $Zr_6O_4(OH)_4$ node, creating a nondefective MOF; accordingly, reduction of the linker to a 10- and 8-linker by the nonlinker formate modulator will create two or four defect sites per $Zr_6O_4(OH)_4$ node, respectively (Scheme 1). In this regard, our MOF could potentially provide four defect sites per $Th_6O_4(OH)_4$ node, as each $Th_6O_4(OH)_4$ node is surrounded by eight L^{2-} linkers and four nonlinker formate modulators; however, in fact, our MOF can potentially provide eight defect sites per $Th_6O_4(OH)_4$ node, because there also exist four additional linker-type formate modulators that can be further considered as potential defect sites. In the literature, a similar phenomenon has never been observed.

The activity of the defect site in **MOF-Th-Co-66** was confirmed by replacement with acetate. The acetate-replaced phase, namely, **MOF-Th-Co-67**, was obtained by soaking the crystals of **MOF-Th-Co-66** in acetic acid solution for 3 days. The structure of **MOF-Th-Co-67** was determined by single-crystal X-ray diffraction, giving the same tetragonal system with *I4/m* space group as observed in **MOF-Th-Co-66**. No detectable change in the unit cell is observed after acetate replacement. Impressively, in **MOF-Th-Co-67**, we observed complete replacement of formate (composed of both nonlinkers and linkers) by acetate, confirming eight defect sites in **MOF-Th-Co-66** (Figure 2). The aperture of the $Th_{36}Co_4$ cage is reduced to 0.84 nm in **MOF-Th-Co-67**. Moreover, propionate used as the modulator was explored, and the results are shown in Figure S3.

The thermal stability of **MOF-Th-Co-66** and **MOF-Th-Co-67** was initially investigated by a TGA test (Figure S4). The loss of solvent molecules occurs before 100 °C for both **MOF-Th-Co-66** and **MOF-Th-Co-67**. Their activated samples can be obtained first by CH_3OH exchange and then by degassing at 100 °C for 24 h. The porosity was confirmed by N_2 adsorption at 77 K (Figure 3a), suggesting their microporous structure. Their BET values are 690 and 568 m^2/g, respectively. The corresponding pore size distributions are 0.86 and 0.77 nm, respectively, which is consistent with the results estimated from the structural data. The pore volumes are 0.28 and 0.22 cm^3/g, respectively.

SO_2 adsorption isotherms of **MOF-Th-Co-66** and **MOF-Th-Co-67** are shown in Figure 3b. The adsorption capacity at 1 bar and 298 K is 5.00 mmol/g for **MOF-Th-Co-66** and 6.23 mmol/g for **MOF-Th-Co-67**, indicative of a 1.24-fold enhancement in the SO_2 uptake through defect engineering. The uptake exceeds those of commercial activated carbon (3.3

https://doi.org/10.1021/acs.inorgchem.2c03177
Inorg. Chem. 2022, 61, 16986−16991

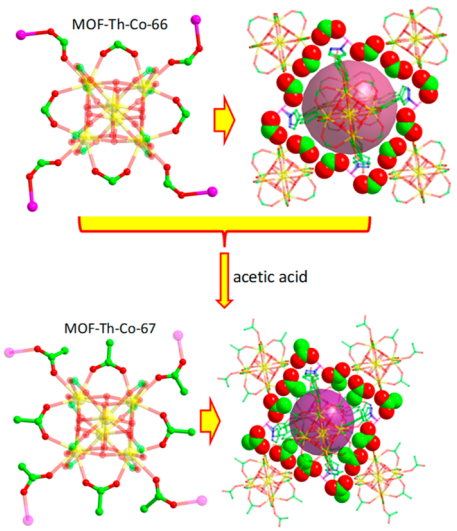

Figure 2. Structural comparison between **MOF-Th-Co-66** and **MOF-Th-Co-67** in the aspects of the $Th_6O_4(OH)_4$ cluster and $Th_{36}Co_4$ cage.

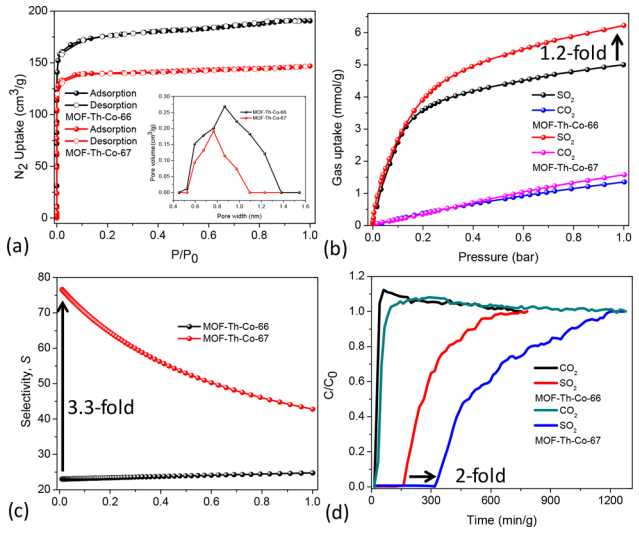

Figure 3. (a) N_2 adsorption isotherms at 77 K with an inset of the corresponding pore size distribution. (b) SO_2 and CO_2 adsorption isotherms at 298 K. (c) SO_2/CO_2 adsorption selectivity at 298 K. (d) Breakthrough curves at 298 K.

mmol/g) and 13X zeolite (2.7 mmol/g) and is comparable with the benchmark MOF of SIFSIX-2−Cu-I (6.90 mmol/g).[47] By contrast, they afford low CO_2 uptake such as 1.35 mmol/g for **MOF-Th-Co-66** and 1.58 mmol/g for **MOF-Th-Co-67**, strongly suggesting selective adsorption of SO_2 over CO_2.

We further employ the commonly used IAST method (ideal adsorbed solution theory) to estimate the SO_2/CO_2 selectivity.[50−56] It is found that **MOF-Th-Co-67** shows higher SO_2/CO_2 selectivity over **MOF-Th-Co-66** (Figure 3c). At 1 bar and 298 K, **MOF-Th-Co-67** gives a selectivity of 42.78, far exceeding **MOF-Th-Co-66** with a selectivity of 24.75, creating a 1.7-fold enhancement in SO_2/CO_2 selectivity. More impressively, the selectivity at the onset of adsorption is up to 76.6 for **MOF-Th-Co-67**, almost 3.3-fold that for **MOF-Th-Co-66** (S = 23.01). The selectivity (S = 76.61−42.78) of **MOF-Th-Co-67** is comparable with some benchmark MOFs such as MFM-601 (67.5−36.2), SIFSIX-1-Cu (70.7−54.1), and SIFSIX-2-Cu-i (89.4−87.1).[47−54] The results imply stronger host−guest interactions for **MOF-Th-Co-67** over **MOF-Th-Co-66**. Q_{st} is used to reflect the host−guest interaction between the MOF and gas molecules.[50−56] In light of the adsorption data at 298 and 273 K, their Q_{st} values are obtained (Figures S5 and S6). The Q_{st} of SO_2 (35.83 kJ/mol) in **MOF-Th-Co-67** is bigger than that of 28.39 kJ/mol in **MOF-Th-Co-66** and comparable with the benchmark materials of MFM-601,[55] while the Q_{st} of CO_2 shows the opposite trend with a hierarchy of **MOF-Th-Co-67** (20.7 kJ/mol) < **MOF-Th-Co-66** (24 kJ/mol). The results imply stronger framework−SO_2 and weaker framework−CO_2 interactions in **MOF-Th-Co-67** over **MOF-Th-Co-66**, thus leading to higher SO_2/CO_2 selectivity in **MOF-Th-Co-67** over **MOF-Th-Co-66**.

To evaluate their actual desulfurization ability, dynamic breakthrough experiments were carried out with SO_2/CO_2 mixtures containing 2000 ppm SO_2 at 298 K (Figure 3d). It is found that CO_2 breaks out from the MOF column immediately, while a long retention time was observed for SO_2 such as 157 min/g for **MOF-Th-Co-66** and 317 min/g for **MOF-Th-Co-67**, implying the excellent separation of trace SO_2 from the SO_2/CO_2 mixture. Impressively, in contrast to that in **MOF-Th-Co-66**, the retention time for SO_2 in **MOF-Th-Co-67** is enhanced by 2-fold. In addition, both MOFs displayed no evident loss in SO_2 retention time in the second and third run of the regenerated MOFs (Figures S7 and S8). PXRD was further used to confirm the stability of the two MOFs after breakthrough tests (Figures S9 and S10).

The adsorption mechanism of SO_2 on the two MOFs was initially investigated by Grand Canonical Monte Carlo (GCMC) simulations of SO_2 adsorption.[56] The calculated SO_2 adsorption isotherms at 298 K are comparable with the experimental value (Figures S11 and S12). The sorption density of SO_2 was analyzed, and one major as well as one minor sorption site were disclosed, the major located at the window of the $Th_{36}Co_4$ cage and the minor located in the pore of the $Th_{36}Co_4$ cage (Figures S13 and S14). Details were further elucidated by using periodic dispersion-corrected DFT (DFT-D) calculations (Figure S15).[56] For **MOF-Th-Co-66**, site I is close to one nonlinker formate modulator with $(C)H(^{\delta+})\cdots(^{\delta-})O(S)$ interactions (Figure S15a,b). The O···H distance is 2.89 Å. This site is further stabilized by both $(C)H(^{\delta+})\cdots(^{\delta-})O(S)$ interactions (2.96 Å) and benzene$(^{\delta-})\cdots(^{\delta+})S$ interactions (3.72 Å, 3.81 Å) between SO_2 and L^{2-} ligands. The binding energy is −27.77 kJ/mol. By contrast, site II is close to one linker-type formate modulator, and just stabilized by $(C)H(^{\delta+})\cdots(^{\delta-})O(S)$ interaction with an O···H distance of 1.99 Å (Figure S15a,b), thus giving a small binding energy of −10.54 kJ/mol. By contrast, for **MOF-Th-Co-67**, we observed multiple $(C)H(^{\delta+})\cdots(^{\delta-})O(S)$ interactions among SO_2, acetate, and L^{2-} ligands (3.02−3.38 Å) (Figure S15c), thus leading to a higher binding energy of −30.62 kJ/mol relative to that in **MOF-Th-Co-66**. Site II in **MOF-Th-Co-67** is also strengthened by two $(C)H(^{\delta+})\cdots(^{\delta-})O(S)$ interactions with an O···H distance of 1.73 Å from one linker-type acetate modulator and 2.94 Å from one nonlinker acetate modulator (Figure S15d). Accordingly, the binding energy is enhanced up to −22.22 kJ/mol, relative to that in **MOF-Th-Co-66**.

In summary, we demonstrate herein a single-crystal defective MOF through a bimetallic approach, resulting in a record eight defect sites per metal node. The application of this defective

https://doi.org/10.1021/acs.inorgchem.2c03177
Inorg. Chem. 2022, 61, 16986−16991

MOF was initially reflected in the removal of trace SO_2 with high adsorption capacity and SO_2/CO_2 selectivity. Further, this MOF could be potentially used in catalysis, separation, and so on, when a suitable modulator is used.

■ ASSOCIATED CONTENT

Supporting Information

The Supporting Information is available free of charge at https://pubs.acs.org/doi/10.1021/acs.inorgchem.2c03177.

Synthesis details and additional figures including PXRD patterns, structures, TG plots, Q_{st} values, breakthrough test results, and SO_2 and CO_2 adsorption (PDF)

Accession Codes

CCDC 2131573−2131574 contain the supplementary crystallographic data for this paper. These data can be obtained free of charge via www.ccdc.cam.ac.uk/data_request/cif, or by emailing data_request@ccdc.cam.ac.uk, or by contacting The Cambridge Crystallographic Data Centre, 12 Union Road, Cambridge CB2 1EZ, UK; fax: +44 1223 336033.

■ AUTHOR INFORMATION

Corresponding Authors

Xue Feng Feng − *School of Biology, Chemistry and Material Science,, East China University of Technology, Nanchang, Jiangxi 344000, China*; Email: xffeng@ecut.cn

Feng Luo − *School of Biology, Chemistry and Material Science,, East China University of Technology, Nanchang, Jiangxi 344000, China*; orcid.org/0000-0001-6380-2754; Email: ecitluofeng@163.com

Authors

Hui Ping Zhang − *School of Biology, Chemistry and Material Science,, East China University of Technology, Nanchang, Jiangxi 344000, China*

Qing Yun Zhang − *School of Biology, Chemistry and Material Science,, East China University of Technology, Nanchang, Jiangxi 344000, China*

Rajamani Krishna − *Van't Hoff Institute for Molecular Sciences, University of Amsterdam, 1098 XH Amsterdam, The Netherlands*; orcid.org/0000-0002-4784-8530

Complete contact information is available at: https://pubs.acs.org/10.1021/acs.inorgchem.2c03177

Author Contributions

The manuscript was written through contributions of all authors.

Notes

The authors declare no competing financial interest.

■ ACKNOWLEDGMENTS

We thank the Training Program for Academic and Technical Leaders of Major Disciplines in Jiangxi Province (20194BCJ22010), the National Natural Science Foundations of China (21966002 and 21871047), the Youth leading talent project of FuZhou (2020ED64), and Jiangxi Project DHSQT22021007.

■ REFERENCES

(1) Bennett, T. D.; Cheetham, A. K.; Fuchs, A. H.; Coudert, F.-X. Interplay between defects, disorder and flexibility in metal-organic frameworks. *Nat. Chem.* **2017**, *9*, 11−16.

(2) Chen, C. X.; Wei, Z. W.; Jiang, J. J.; Zheng, S. P.; Wang, H. P.; Qiu, Q. F.; Cao, C. C.; Fenske, D.; Su, C. Y. Dynamic spacer installation for multirole metal-organic frameworks: a new direction toward multifunctional MOFs achieving ultrahigh methane storage working capacity. *J. Am. Chem. Soc.* **2017**, *139*, 6034−6037.

(3) Wang, Y.; Liu, Q.; Zhang, Q.; Peng, B.; Deng, H. X. Molecular vise approach to create metal-binding sites in MOFs and detection of biomarkers. *Angew. Chem., Int. Ed.* **2018**, *57*, 7120−7125.

(4) Chen, C. X.; Wei, Z. W.; Pham, T.; Lan, P. C.; Zhang, L.; Forrest, K. A.; Chen, S.; Al-Enizi, A. M.; Nafady, A.; Su, C. Y.; Ma, S. Q. Nanospace engineering of metal−organic frameworks through dynamic spacer installation of multifunctionalities for efficient separation of ethane from ethane/ethylene mixtures. *Angew. Chem. Int. Ed.* **2021**, *60*, 9680−9685.

(5) Dissegna, S.; Epp, K.; Heinz, W. R.; Kieslich, G.; Fischer, R. A. Metal−organic frameworks: defective metal-organic frameworks. *Adv. Mater.* **2018**, *30*, 1704501−1704524.

(6) Ejegbavwo, O. A.; Martin, C. R.; Olorunfemi, O. A.; Leith, G. A.; Ly, R. T.; Rice, A. M.; Dolgopolova, E. A.; Smith, M. D.; Karakalos, S. G.; Birkner, N.; Powell, B. A.; Pandey, S.; Koch, R. J.; Misture, S. T.; zur Loye, H. C.; Phillpot, S. R.; Brinkman, K. S.; Shustova, N. B. Thermodynamics and electronic properties of heterometallic multinuclear actinide-containing metal-organic frameworks with "structural memory. *J. Am. Chem. Soc.* **2019**, *141*, 11628−11640.

(7) Feng, H.; Xiong, X. H.; Gong, L. L.; Zhang, H. P.; Xu, Y.; Feng, X. F.; Luo, F. Rational tuning of thorium-organic frameworks by reticular chemistry for boosting radionuclide sequestration. *Nano Res.* **2022**, *15*, 1472−1478.

(8) Luo, Y.; Ahmad, M.; Schug, A.; Tsotsalas, M. J. A. M. Rising up: hierarchical metal−organic frameworks in experiments and simulations. *Adv. Mater.* **2019**, *31*, 1901744.

(9) Khan, N. A.; Hasan, Z.; Jhung, S. H. Beyond pristine metal-organic frameworks: preparation and application of nanostructured, nanosized, and analogous MOFs. *Coor. Chem. Rev.* **2018**, *376*, 20−45.

(10) (a) Feng, D. W.; Gu, Z. Y.; Li, J. R.; Jiang, H. L.; Wei, Z. W.; Zhou, H. C. Zirconium-metalloporphyrin PCN-222: mesoporous metal−organic frameworks with ultrahigh stability as biomimetic catalysts. *Angew. Chem., Int. Ed.* **2012**, *51*, 10307−10310. (b) Gao, J.; Qian, X.; Lin, R.; Krishna, R.; Wu, H.; Zhou, W.; Chen, B. Mixed metal-organic framework with multiple binding sites for efficient C_2H_2/CO_2 separation. *Angew. Chem., Int. Ed.* **2020**, *59*, 4396−4400. (c) Xu, H.; Zhong, F.; Chen, F.; Luan, T.; Li, P.; Xu, S.; Gao, J. A Zr-MOF nanoflower sensor and its mixed-matrix membrane for the highly sensitive detection of nitroaromatics. *J. Mater. Chem. C* **2022**, *10*, 7469−7475.

(11) Mondloch, J. E.; Bury, W.; Fairen-Jimenez, D.; Kwon, S.; DeMarco, E. J.; Weston, M. H.; Sarjeant, A. A.; Nguyen, S. T.; Stair, P. C.; Snurr, R. Q.; Farha, O. K.; Hupp, J. T. Vapor-phase metalation by atomic layer deposition in a metal−organic framework. *J. Am. Chem. Soc.* **2013**, *135*, 10294−10297.

(12) Li, P.; Vermeulen, N. A.; Malliakas, C. D.; Gómez-Gualdrón, D. A.; Howarth, A. J.; Mehdi, B. L.; Dohnalkova, A.; Browning, N. D.; O'Keeffe, M.; Farha, O. K. Bottom-up construction of a superstructure in a porous uranium-organic crystal. *Science* **2017**, *356*, 624−627.

(13) Yue, Y. F.; Fulvio, P. F.; Dai, S. Hierarchical metal−organic framework hybrids: perturbation-assisted nanofusion synthesis. *Acc. Chem. Res.* **2015**, *48*, 3044−3052.

(14) Yue, Y. F.; Qiao, Z. A.; Fulvio, P. F.; Binder, A. J.; Tian, C. C.; Chen, J. H.; Nelson, K. M.; Zhu, X.; Dai, S. Template-free synthesis of hierarchical porous metal−organic frameworks. *J. Am. Chem. Soc.* **2013**, *135*, 9572−9575.

(15) Huang, H. L.; Li, J. R.; Wang, K. K.; Han, T. T.; Tong, M. M.; Li, L. S.; Xie, Y. B.; Yang, Q. Y.; Liu, D. H.; Zhong, C. L. An in situ self-assembly template strategy for the preparation of hierarchical-pore metal-organic frameworks. *Nat. Commun.* **2015**, *6*, 8847.

(16) Sun, L. B.; Li, J. R.; Park, J.; Zhou, H. C. Cooperative template-directed assembly of mesoporous metal−organic frameworks. *J. Am. Chem. Soc.* **2012**, *134*, 126−129.

(17) Qiu, L. G.; Xu, T.; Li, Z. Q.; Wang, W.; Wu, Y.; Jiang, X.; Tian, X. Y.; Zhang, L. D. Hierarchically micro- and mesoporous metal−organic frameworks with tunable porosity. *Angew. Chem., Int. Ed.* **2008**, *47*, 9487−9491.
(18) Zhao, Y. J.; Zhang, J. L.; Han, B. X.; Song, J. L.; Li, J. S.; Wang, Q. A. Metal−organic framework nanospheres with well-ordered mesopores synthesized in an ionic liquid/CO_2/surfactant system. *Angew. Chem., Int. Ed.* **2011**, *50*, 636−639.
(19) Cai, G. R.; Jiang, H. L. A modulator-induced defect-formation strategy to hierarchically porous metal−organic frameworks with high stability. *Angew. Chem., Int. Ed.* **2017**, *56*, 563−567.
(20) Wee, L. H.; Wiktor, C.; Turner, S.; Vanderlinden, W.; Janssens, N.; Bajpe, S. R.; Houthoofd, K.; Van Tendeloo, G.; De Feyter, S.; Kirschhock, C. E. A.; Martens, J. A. Copper benzene tricarboxylate metal−organic framework with wide permanent mesopores stabilized by keggin polyoxometallate Ions. *J. Am. Chem. Soc.* **2012**, *134*, 10911−10919.
(21) Vermoortele, F.; Bueken, B.; Le Bars, G.; Van de Voorde, B.; Vandichel, M.; Houthoofd, K.; Vimont, A.; Daturi, M.; Waroquier, M.; Van Speybroeck, V.; Kirschhock, C.; De Vos, D. E. Synthesis modulation as a tool to increase the catalytic activity of metal−organic frameworks: the unique case of UiO-66(Zr). *J. Am. Chem. Soc.* **2013**, *135*, 11465−11468.
(22) Yang, D.; Ortuño, M. A.; Bernales, V.; Cramer, C. J.; Gagliardi, L.; Gates, B. C. Structure and dynamics of Zr_6O_8 metal−organic framework node surfaces probed with ethanol dehydration as a catalytic test reaction. *J. Am. Chem. Soc.* **2018**, *140*, 3751−3759.
(23) Jain, J. R.; Pillai, C. N. Catalytic dehydration of alcohols over alumina: mechanism of ether formation. *J. Catal.* **1967**, *9*, 322−330.
(24) Zhang, J. Z.; An, B.; Li, Z.; Cao, Y. H.; Dai, Y. H.; Wang, W. Y.; Zeng, L. Z.; Lin, W. B.; Wang, C. Neighboring Zn−Zr sites in a metal−organic framework for CO_2 hydrogenation. *J. Am. Chem. Soc.* **2021**, *143*, 8829−8837.
(25) Ma, X.; Liu, H.; Yang, W. J.; Mao, G. Y.; Zheng, L. R.; Jiang, H. L. Modulating coordination environment of single-atom catalysts and their proximity to photosensitive units for boosting MOF photocatalysis. *J. Am. Chem. Soc.* **2021**, *143*, 12220−12229.
(26) Ma, Y. J.; Han, X.; Xu, S. J.; Wang, Z.; Li, W. Y.; da Silva, I.; Chansai, S.; Lee, D.; Zou, Y. C.; Nikiel, M.; Manuel, P.; Sheveleva, A. M.; Tuna, F.; McInnes, E. J. L.; Cheng, Y. Q.; Rudić, S.; Ramirez-Cuesta, A. J.; Haigh, S. J.; Hardacre, C.; Schröder, M.; Yang, S. H. Atomically dispersed copper sites in a metal−organic framework for reduction of nitrogen dioxide. *J. Am. Chem. Soc.* **2021**, *143*, 10977−10985.
(27) Yeh, B.; Vicchio, S. P.; Chheda, S.; Zheng, J.; Schmid, J. L.; Löbbert, L.; Bermejo-Deval, R.; Gutiérrez, O. Y.; Lercher, J. A.; Lu, C. C.; Neurock, M.; Getman, R. B.; Gagliardi, L.; Bhan, A. Site densities, rates, and mechanism of stable Ni/UiO-66 ethylene oligomerization catalysts. *J. Am. Chem. Soc.* **2021**, *143*, 20274−20280.
(28) Nguyen, H. G. T.; Schweitzer, N. M.; Chang, C. Y.; Drake, T.; So, L. M. C.; Stair, P. C.; Farha, O. K.; Hupp, J. T.; Nguyen, S. T. Vanadium-node-functionalized UiO-66: a thermally stable MOF-supported catalyst for the gas-phase oxidative dehydrogenation of cyclohexene. *ACS Catal.* **2014**, *4*, 2496−2500.
(29) Abdel-Mageed, A. M.; Rungtaweevoranit, B.; Parlinska-Wojtan, M.; Pei, X.; Yaghi, O. M.; Behm, R. J. Highly active and stable single-atom Cu catalysts supported by a metal−organic framework. *J. Am. Chem. Soc.* **2019**, *141*, 5201−5210.
(30) Yoskamtorn, T.; Zhao, P.; Wu, X. P.; Purchase, K.; Orlandi, F.; Manuel, P.; Taylor, J.; Li, Y. Y.; Day, S.; Ye, L.; Tang, C. C.; Zhao, Y. F.; Edman Tsang, S. C. Responses of defect-rich Zr-based metal−organic frameworks toward NH_3 adsorption. *J. Am. Chem. Soc.* **2021**, *143*, 3205−3218.
(31) Shearer, G. C.; Chavan, S.; Bordiga, S.; Svelle, S.; Olsbye, U.; Lillerud, K. P. Defect engineering: tuning the porosity and composition of the metal−organic framework UiO-66 via modulated synthesis. *Chem. Mater.* **2016**, *28*, 3749−3761.
(32) Shearer, G. C.; Chavan, S.; Ethiraj, J.; Vitillo, J. G.; Svelle, S.; Olsbye, U.; Lamberti, C.; Bordiga, S.; Lillerud, K. P. Tuned to perfection: ironing out the defects in metal−organic framework UiO-66. *Chem. Mater.* **2014**, *26*, 4068−4071.
(33) Feng, X.; Hajek, J.; Jena, H. S.; Wang, G.; Veerapandian, S. K. P.; Morent, R.; De Geyter, N.; Leyssens, K.; Hoffman, A. E. J.; Meynen, V.; Marquez, C.; De Vos, D. E.; Van Speybroeck, V.; Leus, K.; Voort, P. V. D. Engineering a highly defective stable UiO-66 with tunable lewis-brønsted acidity: the role of the hemilabile linker. *J. Am. Chem. Soc.* **2020**, *142*, 3174−3183.
(34) Bai, Y.; Dou, Y.; Xie, L. H.; Rutledge, W.; Li, J. R.; Zhou, H. C. Zr-based metal−organic frameworks: design, synthesis, structure, and applications. *Chem. Soc. Rev.* **2016**, *45*, 2327−2367.
(35) Cavka, J. H.; Jakobsen, S.; Olsbye, U.; Guillou, N.; Lamberti, C.; Bordiga, S.; Lillerud, K. P. A new zirconium inorganic building brick forming metal organic frameworks with exceptional stability. *J. Am. Chem. Soc.* **2008**, *130*, 13850−13851.
(36) Trickett, C. A.; Gagnon, K. J.; Lee, S.; ndara, F. G.; Bügi, H.-B.; Yaghi, O. M. Definitive molecular level characterization of defects in UiO-66 crystals. *Angew. Chem., Int. Ed.* **2015**, *54*, 11162−11167.
(37) Wu, H.; Chua, Y. S.; Krungleviciute, V.; Tyagi, M.; Chen, P.; Yildirim, T.; Zhou, W. Unusual and highly tunable missing-linker defects in zirconium metal−organic framework UiO-66 and their important effects on gas adsorption. *J. Am. Chem. Soc.* **2013**, *135*, 10525−10532.
(38) Valenzano, L.; Civalleri, B.; Chavan, S.; Bordiga, S.; Nilsen, M. H.; Jakobsen, S.; Lillerud, K. P.; Lamberti, C. Disclosing the complex structure of UiO-66 metal organic framework: a synergic combination of experiment and theory. *Chem. Mater.* **2011**, *23*, 1700−1718.
(39) Katz, M. J.; Brown, Z. J.; Colyn, Y. J.; Siu, P. W.; Scheidt, K. A.; Snurr, R. Q.; Hupp, J. T.; Farha, O. K. A facile synthesis of UiO-66, UiO-67 and their derivatives. *Chem. Commun.* **2013**, *49*, 9449−9451.
(40) Atzori, C.; Shearer, G. C.; Maschio, L.; Civalleri, B.; Bonino, F.; Lamberti, C.; Svelle, S.; Lillerud, K. P.; Bordiga, S. J. Phys. Effect of benzoic acid as a modulator in the structure of UiO-66: an experimental and computational study. *J. Phys. Chem. C* **2017**, *121*, 9312−9324.
(41) Ameloot, R.; Vermoortele, F.; Hofkens, J.; De Schryver, F. C.; De Vos, D. E.; Roeffaers, M. B. J. Three-dimensional visualization of defects formed during the synthesis of metal−organic frameworks: a fluorescence microscopy study. *Angew. Chem., Int. Ed.* **2013**, *52*, 401−405.
(42) Schrimpf, W.; Jiang, J.; Ji, Z.; Hirschle, P.; Lamb, D. C.; Yaghi, O. M.; Wuttke, S. Chemical diversity in a metal−organic framework revealed by fluorescence lifetime imaging. *Nat. Commun.* **2018**, *9*, 1−10.
(43) Shöâeè, M.; Agger, J. R.; Anderson, M. W.; Attfield, M. P. Crystal form, defects and growth of the metal organic framework HKUST-1 revealed by atomic force microscopy. *CrystEngComm* **2008**, *10*, 646−648.
(44) Johnstone, D. N.; Firth, F. C. N.; Grey, C. P.; Midgley, P. A.; Cliffe, M. J.; Collins, S. M. Direct imaging of correlated defect nanodomains in a metal−organic framework. *J. Am. Chem. Soc.* **2020**, *142*, 13081−13089.
(45) Blatov, V. A. *TOPOS*; Samara, Russia, 2006. http://www.topos.ssu.samara.ru.
(46) Blatov, V. A.; Shevchenko, A. P.; Serezhkin, V. N. TOPOS3.2: A new version of the program package for multipurpose crystal-chemical analysis. *J. Appl. Crystallogr.* **2000**, *33*, 1193.
(47) Cui, X. L.; Yang, Q. W.; Yang, L. F.; Krishna, R.; Zhang, Z. G.; Bao, Z. B.; Wu, H.; Ren, Q. L.; Zhou, W.; Chen, B. L.; Xing, H. B. Gas purification: ultrahigh and selective SO_2 uptake in inorganic anion-pillared hybrid porous materials. *Adv. Mater.* **2017**, *29*, 1606929.
(48) Yang, S.; Sun, J.; Ramirez-Cuesta, A. J.; Callear, S. K.; David, W. I. F.; Anderson, D. P.; Newby, R.; Blake, A. J.; Parker, J. E.; Tang, C. C.; Schroder, M. Selectivity and direct visualization of carbon dioxide and sulfur dioxide in a decorated porous host. *Nat. Chem.* **2012**, *4*, 887.
(49) Savage, M.; Cheng, Y.; Easun, T. L.; Eyley, J. E.; Argent, S. P.; Warren, M. R.; Lewis, W.; Murray, C.; Tang, C. C.; Frogley, M. D.; Cinque, G.; Sun, J.; Rudić, S.; Murden, R. T.; Benham, M. J.; Fitch, A.

https://doi.org/10.1021/acs.inorgchem.2c03177
Inorg. Chem. 2022, 61, 16986−16991

N.; Blake, A. J.; Ramirez-Cuesta, A. J.; Yang, S.; Schroder, M. Selective adsorption of sulfur dioxide in a robust metal−organic framework material. *Adv. Mater.* **2016**, *28*, 8705.
(50) Tan, K.; Canepa, P.; Gong, Q.; Liu, J.; Johnson, D. H.; Dyevoich, A.; Thallapally, P. K.; Thonhauser, T.; Li, J.; Chabal, Y. J. Mechanism of preferential adsorption of SO_2 into two microporous paddle wheel frameworks $M(bdc)(ted)_{0.5}$. *Chem. Mater.* **2013**, *25*, 4653.
(51) Xing, S. H.; Liang, J.; Brandt, P.; Sch-fer, F.; Nuhnen, A.; Heinen, T.; Boldog, I.; Mçllmer, J.; Lange, M.; Weingart, O.; Janiak, C. Capture and separation of SO_2 traces in metal−organic frameworks via pre-synthetic pore environment tailoring by methyl groups. *Angew. Chem., Int. Ed.* **2021**, *60*, 17998−18005.
(52) Martínez-Ahumada, E.; He, D. L.; Berryman, V.; Llpez-Olvera, A.; Hernandez, M.; Jancik, V.; Martis, V.; Vera, M. A.; Lima, E.; Parker, D. J.; Cooper, A. I.; Ibarra, I. A.; Liu, M. Inside back cover: SO_2 capture using porous organic cages. *Angew. Chem., Int. Ed.* **2021**, *60*, 17556−17563.
(53) Grape, E. S.; Flores, J. G.; Hidalgo, T.; Martínez-Ahumada, E.; Gutiérrez-Alejandre, A.; Hautier, A.; Williams, D. R.; O'Keeffe, M.; Willhammar; LarsÖhrström, T.; Horcajada, P.; Ibarra, I. A.; Inge, A. K. A robust and biocompatible bismuth ellagate MOF synthesized under green ambient conditions. *J. Am. Chem. Soc.* **2020**, *142*, 16795−16804.
(54) Chen, F. Q.; Lai, D.; Guo, L. D.; Wang, J.; Zhang, P. X.; Wu, K. Y.; Zhang, Z. G.; Yang, Q. W.; Yang, Y. W.; Chen, B. L.; Ren, Q. L.; Bao, Z. B. Deep desulfurization with record SO_2 adsorption on the metal−organic frameworks. *J. Am. Chem. Soc.* **2021**, *143*, 9040−9047.
(55) Carter, J. H.; Han, X.; Moreau, F. Y.; Silva, I.; Nevin, A.; Godfrey, H. G. W.; Tang, C. C.; Yang, S.; Schröder, M. Exceptional adsorption and binding of sulfur dioxide in a robust zirconium-based metal-organic framework. *J. Am. Chem. Soc.* **2018**, *140*, 15564−15567.
(56) (a) Zhang, H. P.; Fan, Y. L.; Krishna, R.; Feng, X. F.; Wang, L.; Luo, F. Robust metal-organic framework with multiple traps for trace Xe/Kr separation. *Sci. Bull.* **2021**, *66*, 1073−1079. (b) Luo, F.; Yan, C. S.; Dang, L. L.; Krishna, R.; Zhou, W.; Wu, H.; Dong, X. L.; Han, Y.; Hu, T. L.; O'Keeffe, M.; Wang, L. L.; Luo, M. B.; Lin, R. B.; Chen, B. L. UTSA-74: a MOF-74 isomer with two accessible binding sites per metal center for highly selective gas separation. *J. Am. Chem. Soc.* **2016**, *138*, 5678−5684. (c) Yin, M.; Krishna, R.; Wang, W.; Yuan, D.; Fan, Y.; Feng, X.; Wang, L.; Luo, F. A $[Th_8Co_8]$ nanocage-based metal-organic framework with extremely narrow window but flexible nature enabling dual-sieving effect for both isotope and isomer separation. *CCS Chem.* **2022**, *4*, 1016−1027.

https://doi.org/10.1021/acs.inorgchem.2c03177
Inorg. Chem. 2022, 61, 16986−16991

Creating High-Number Defect Site through Bimetal Approach in Metal-Organic Framework for Boosting Trace SO_2 Removal

Hui Ping Zhang, Qing Yun Zhang, Xue Feng Feng,* Rajamani Krishna, and Feng Luo*

Corresponding author: Feng Luo, ecitluofeng@163.com; Xue Feng Feng, xffeng@ecut.cn

Experimental Section

Materials and general methods. *Caution! $Th(NO_3)_4$ used in this study emitts an α emitter, and the use of $Th(NO_3)_4$ was operated in an authorized laboratory designed for actinide element studies. Standard precautions for handling radioactive materials should be followed.* Reagents and solvents were commercially available (Alfa) and were used without further purification. X-ray powder diffraction were collected by a Bruker AXSD8 Discover powder diffractometer at 40 kV, 40 mA for Cu Kλ (λ= 1.5406 Å). The simulated powder patterns were calculated by Mercury 1.4. Infrared Spectra (IR) were measured by a Bruker VERTEX70 spectrometer in the 500-4000 cm^{-1} region. The gas adsorption isotherms were collected on a Belsorp-max. Ultrahigh-purity-grade (>99.999%) N_2, SO_2, and CO_2 gases were used during the adsorption measurement. To maintain the experimental temperatures, liquid nitrogen (77 K) and water/ice bath (298 K and 273 K) was used.

Synthetic procedures

Synthesis of MOF-Th-Co-66. $Th(NO_3)_2 \cdot 4H_2O$ (0.0208 mmol, 10 mg), $Co(NO_3)_2 \cdot 6H_2O$ (0.0344 mmol, 10 mg), 4-(1H-Pyrazol-4-yl)benzoic acid (0.0797 mmol, 15 mg) were dissolved in a mixture solution of N, N´-dimethylformamide (DMF, 4 mL), H_2O (1 mL) and nitric acid (0.1 mL). The solution was moved into a 25 mL Teflon-lined stainless steel vessel and heated at 115 ºC for 3 days, then it was cooled down to room temperature. Pink crystals were obtained and washed with 10 mL DMF for three times. Yield is 93% based on Th. Element analysis (experimental value): C 32.56%, H/2.66%, N/7.56%.

Synthesis of MOF-Th-Co-67. Single crystals (20-50 mg) of MOF-Th-Co-66 with a mixture solution of N, N´-dimethylformamide (DMF, 4 mL), H_2O (1 mL) and glacial acetic acid (0.15 mL) were placed in a 25 mL Teflon-lined stainless steel vessel for SCSC transformation at 115°C for 3 days, then it was cooled down to room temperature. Pink crystals were obtained and washed with 10 mL DMF for three times. Element analysis (experimental value): C 32.89%, H/2.73%, N/7.49%.

The activation of samples before N_2 adsorption. 100 mg samples were immerged in CH_3OH (30 mL) for three days with changing CH_3OH three times every day. Then the samples were transferred to Belsorp-max and 100°C was used to activate the samples about 24 h.

X-ray Crystallography

X-ray diffraction data of **MOF-Th-Co-66** and **MOF-Th-Co-67** was collected at 298 K on a Bruker-Appex (II) diffractometer using graphite monochromated MoKα radiation (λ=0.71073 Å). The data reduction included a correction for Lorentz and polarization effects, with an applied multi-scan absorption correction (SADABS). The crystal structure was solved and refined using the SHELXTL program suite. Direct methods yielded all non-hydrogen atoms, which were refined with

anisotropic thermal parameters. All hydrogen atom positions were calculated geometrically and were riding on their respective atoms. The SQUEEZE subroutine of the PLATON software suite was used to remove the scattering from the highly disordered guest molecules. CCDC 2131573-2131574 contains the supplementary crystallographic data of **MOF-Th-Co-66** and **MOF-Th-Co-67**. The data can be obtained free of charge from the Cambridge Crystallographic Data Centre via www.ccdc.cam.ac.uk/data_ request/cif. A crystallographic summarization was shown in Table S1 and S2.

GCMC and DFT calculation

The single crystal structure of MOF was used as the initial geometric structure for calculation. The charges of the frame and gas molecules are calculated before the adsorption simulation. Using the Peng-Robinson equation of state to convert the fugacity in the simulation, the adsorption capacity of MOF for SO_2 at a 298 K temperature and 0-1 bar pressure and the adsorption isotherm simulation were studied. All GCMC simulations were done with the Sorption module in MS. Using the Universal force field, the equilibration step and the production step were set to 5×10^6 and 5×10^6, respectively, the cutoff radius was set to 15.5 Å, the buffer width was set to 0.5 Å, and the precision was 1×10^{-4} kcal mol^{-1}.

To obtain the adsorption binding energies of the two sites, we optimized and relaxed the original structure and gas molecules by placing them in a unit cell of the same size as the cell body of the original crystal structure. All optimizations are done with the Focite module in MS. According to the adsorption density map, SO_2 gas molecules were introduced into the corresponding pore positions, and then complete structural relaxation occurred. The binding energy formula is $E_{ads}= E_{MOF/SO2}-E_{MOF}-E_{SO2}$**,** where EMOF/X is the total energy of the structure after the MOF adsorbs SO_2, EMOF is the energy before the MOF adsorbs SO_2, and EX is the structural energy of the structure containing only SO_2 molecules.

Fitting of experimental data on pure component isotherms. The isotherm data for SO_2 in MOF-Th-Co-66 and MOF-Th-Co-67at 273 K and 298 K were fitted with the dual-site Langmuir model, where we distinguish two distinct adsorption sites A and B:

$$q = \frac{q_{sat,A} b_A p}{1 + b_A p} + \frac{q_{sat,B} b_B p}{1 + b_B p} \tag{S1}$$

with T-dependent parameters b_A, and b_B

$$b_A = b_{A0} \exp\left(\frac{E_A}{RT}\right); \quad b_B = b_{B0} \exp\left(\frac{E_B}{RT}\right) \tag{S2}$$

For CO_2 in the two MOFs, a single-site Langmuir model is found to be of excellent accuracy.

The unary isotherm fit parameters for SO_2 and CO_2 are provided in Table S and Table S.

Isosteric heat of adsorption

The binding energy is reflected in the isosteric heat of adsorption, Q_{st}, is calculated from the Clausius-Clapeyron equation.

$$Q_{st} = -RT^2 \left(\frac{\partial \ln p}{\partial T} \right)_q \qquad \text{(S3)}$$

IAST calculations of adsorption selectivities and uptake capacities

We consider the separation of binary SO_2/CO_2 1:99 v/v mixtures at 298 K. The adsorption selectivity for SO_2/CO_2 separation is defined by

$$S_{ads} = \frac{q_1/q_2}{p_1/p_2} \qquad \text{(S4)}$$

Breakthrough test. In the dynamic breakthrough experiment, about 0.25 g activated samples (in the column Ø 46 mm×150 mm) was used. The column is backfilled with argon and mounted in the set-up. Before starting each experiment, helium reference gas is flushed through the column and then the gas flow is switched to the desired gas mixture at the same flow rate of 5 mL/min. The gas mixture downstream the column was monitored using a Hiden mass-spectrometer. The desorption of the adsorbed SO_2 and CO_2 was achieved through 5 ml/min N_2 purge after the breakthrough experiment at 100 ˚C. The flow rate for the SO_2/CO_2 mixture is 10 mL/min.

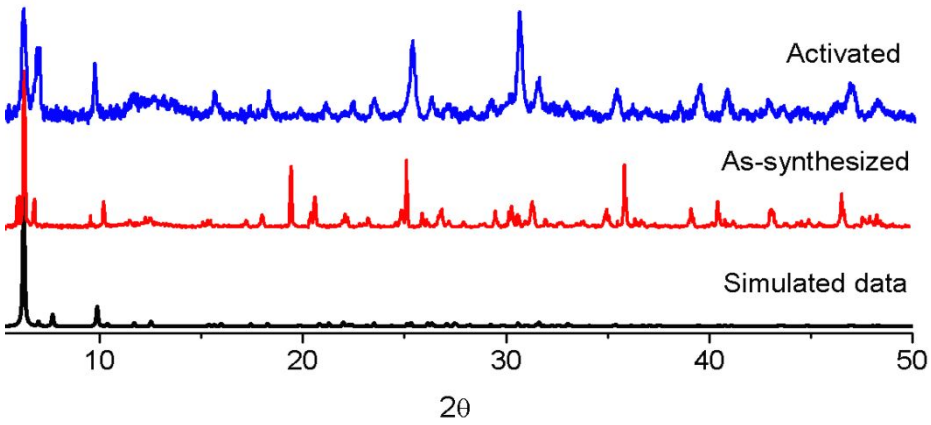

Figure S1. A comparison of PXRD patterns among the simulated data, the as-synthesized samples, and the degassed samples.

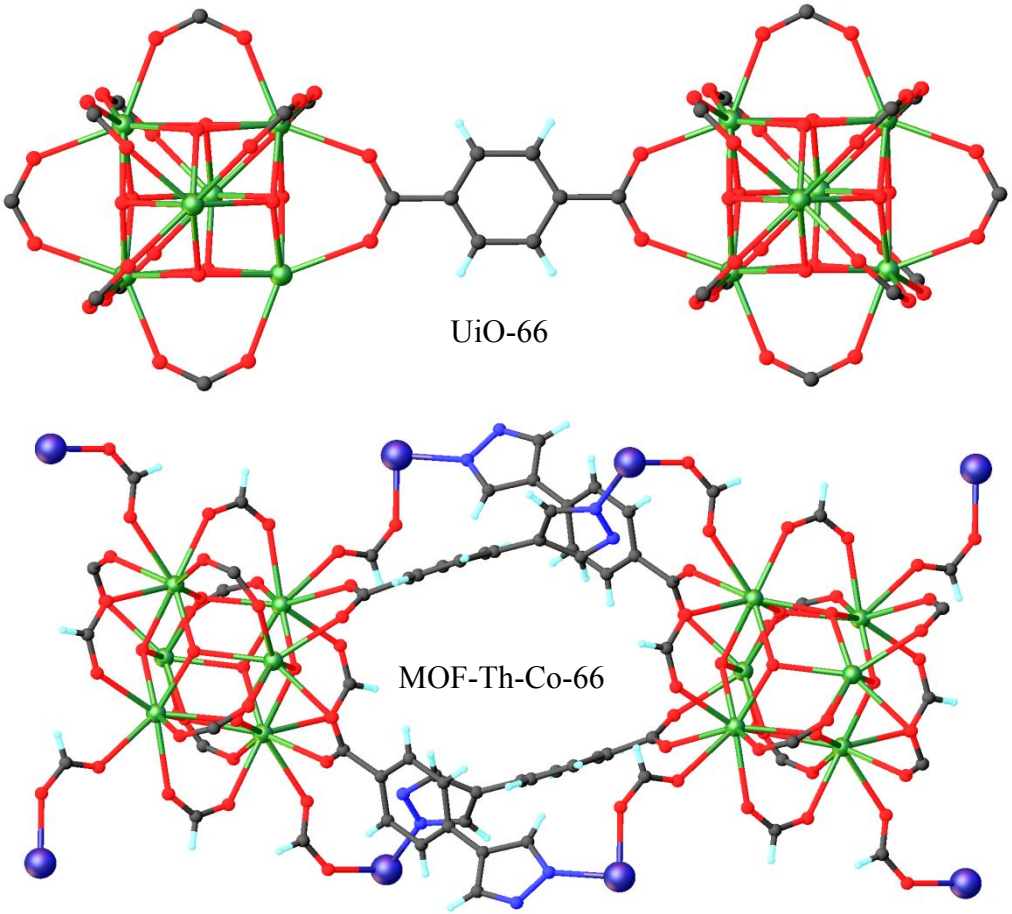

Figure S2. A comparison of connectivity between UiO-66 and our MOF. Clearly, $Zr_6O_4(OH)_4$ clusters in UiO-66 is directly bridged by organic linkers, whereas in our case similar $Th_6O_4(OH)_4$ clusters are not directly bridged by organic linkers, but are bridged by a secondary metal ions.

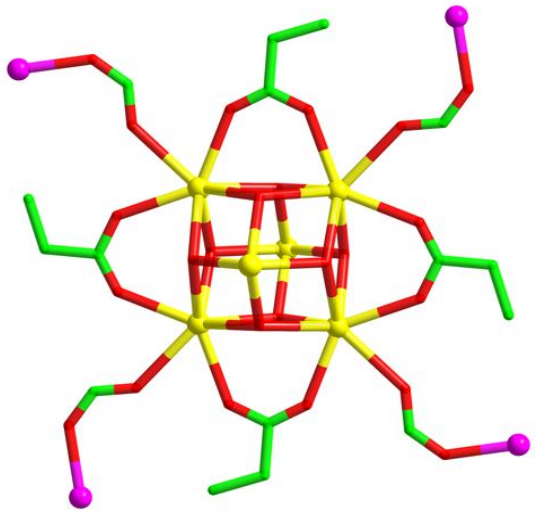

Figure S3. View of the propionate-replaced structure, where clearly just the four non-linker formate modulators was replaced by propionate.

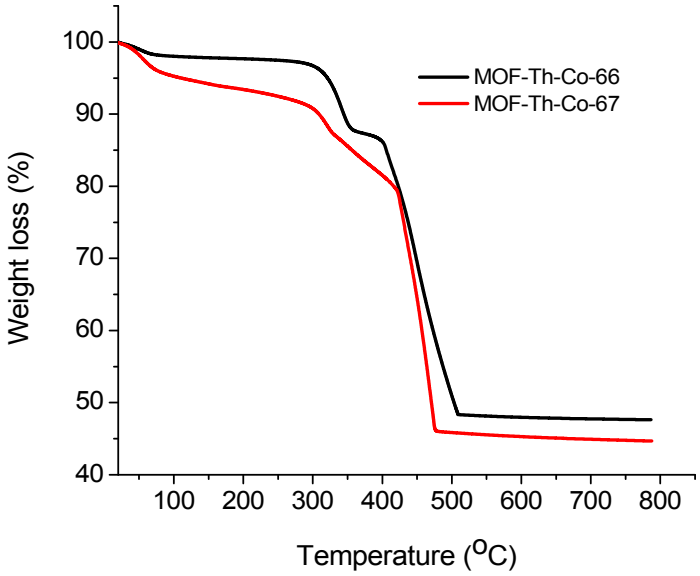

Figure S4. The TG plots of the two MOFs in this work.

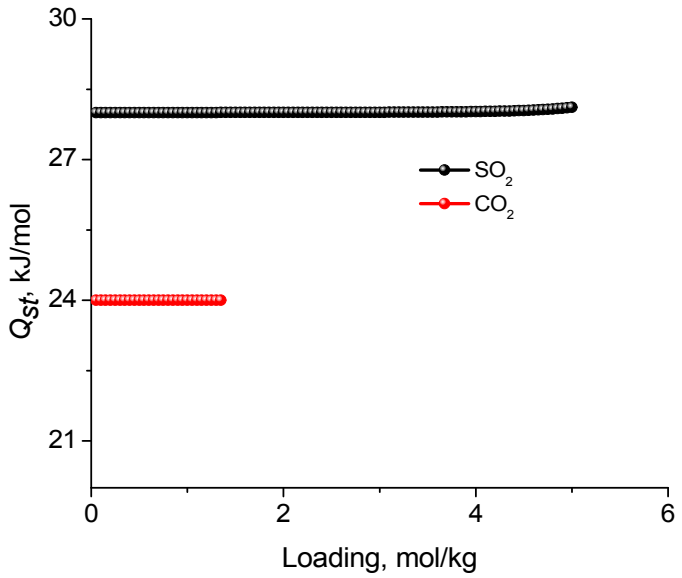

Figure S5. The Qst of SO_2 and CO_2 upon MOF-Th-Co-66.

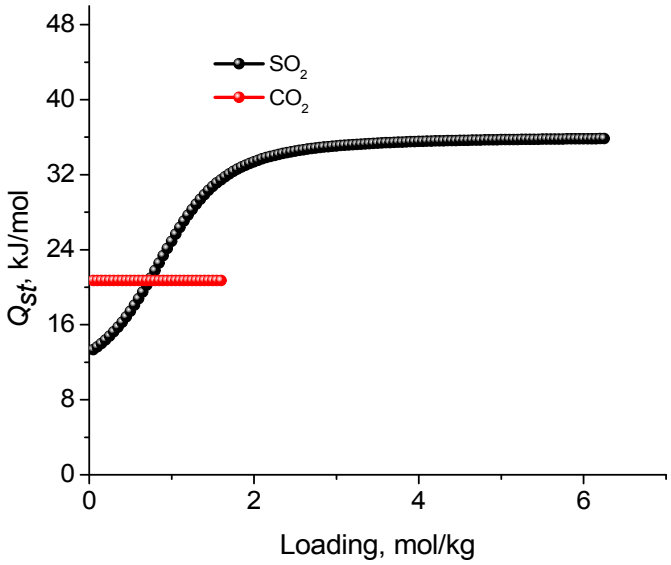

Figure S6. The Qst of SO_2 and CO_2 upon MOF-Th-Co-67.

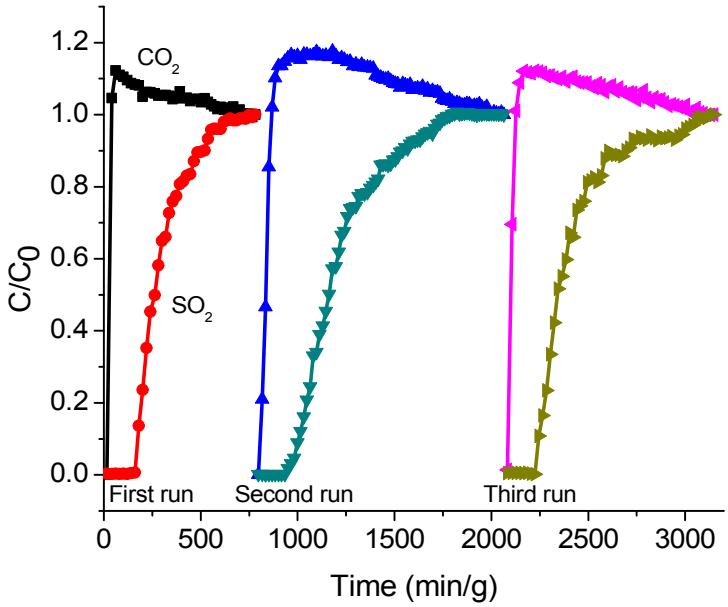

Figure S7. The breakthrough test upon MOF-Th-Co-66 in the first, second and third run for a SO_2/CO_2 mixture containing 2000 ppm SO_2 at 1 bar and 298 K.

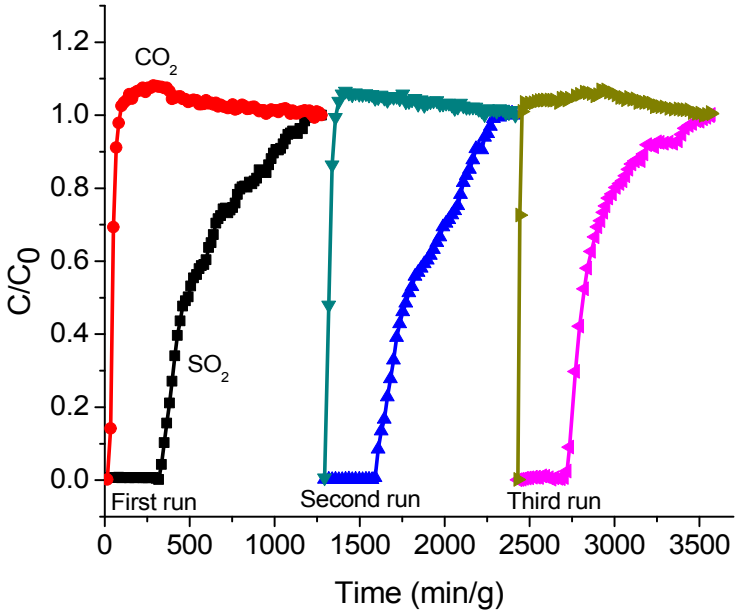

Figure S8. The breakthrough test upon MOF-Th-Co-67 in the first, second and third run for a SO_2/CO_2 mixture containing 2000 ppm SO_2 at 1 bar and 298 K.

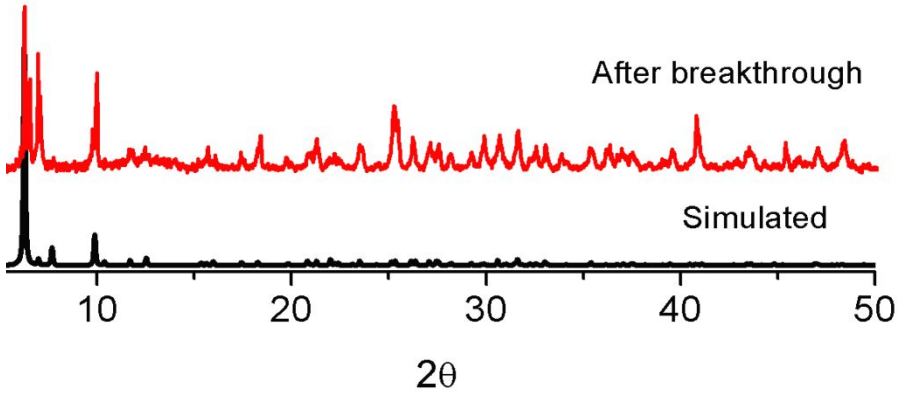

Figure S9. A comparison of PXRD patterns for MOF-Th-Co-66 among the simulated data and the samples after breakthrough test.

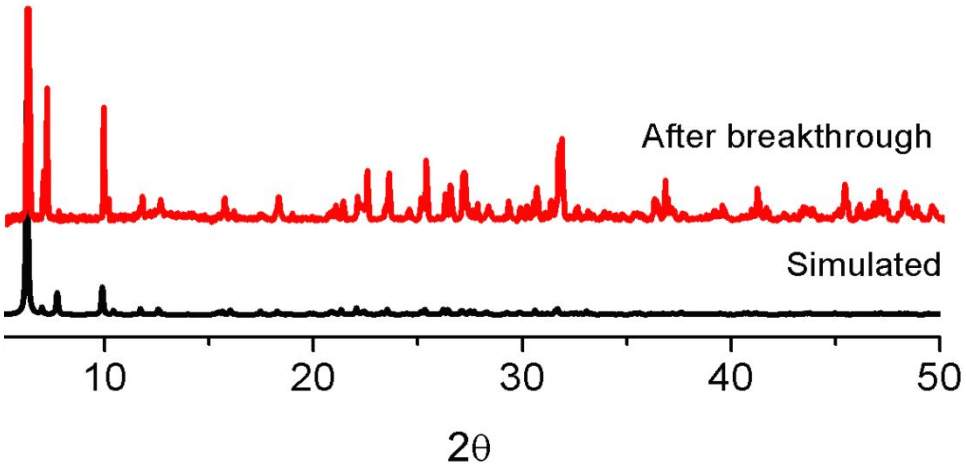

Figure S10. A comparison of PXRD patterns for MOF-Th-Co-67 among the simulated data and the samples after breakthrough test.

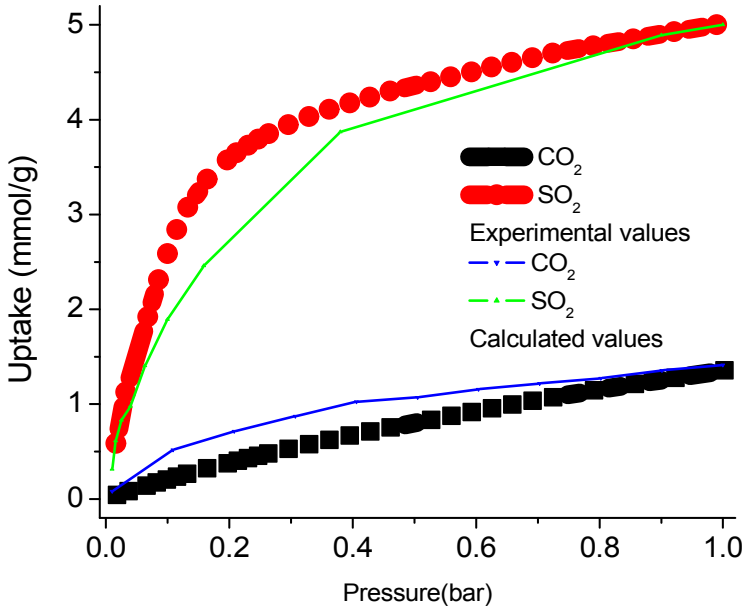

Figure S11. A comparison of experimental and calculated SO_2 and CO_2 adsorption for MOF-Th-Co-66.

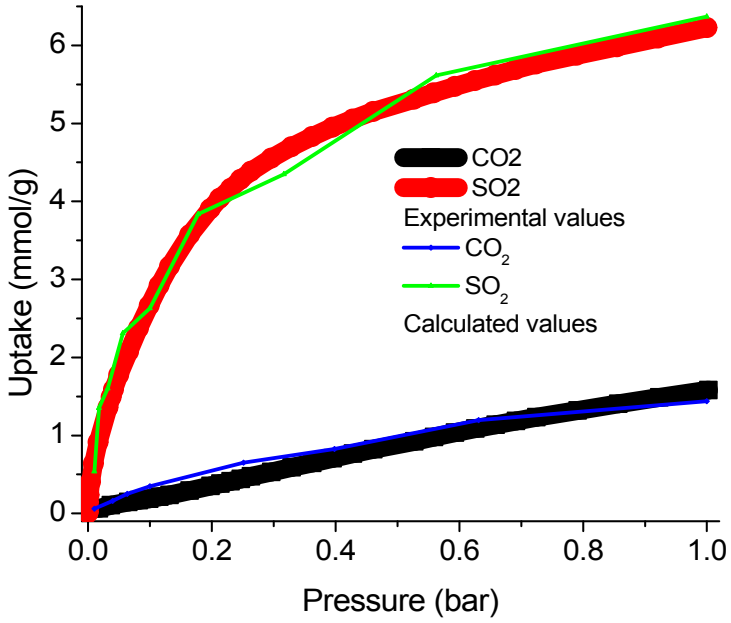

Figure S12. A comparison of experimental and calculated SO_2 and CO_2 adsorption for MOF-Th-Co-67.

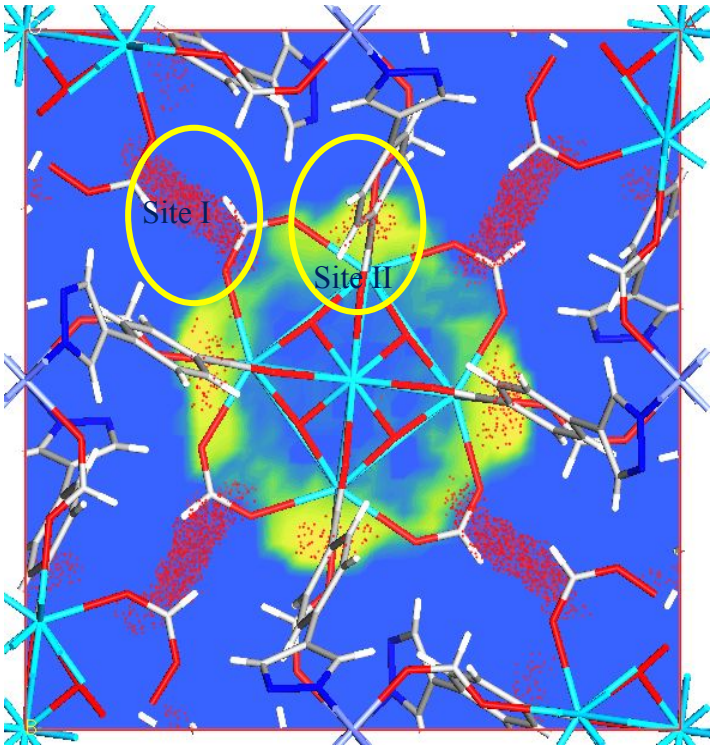

Figure S13. View of the adsorption density of SO_2 in MOF-Th-Co-66 in site I and II.

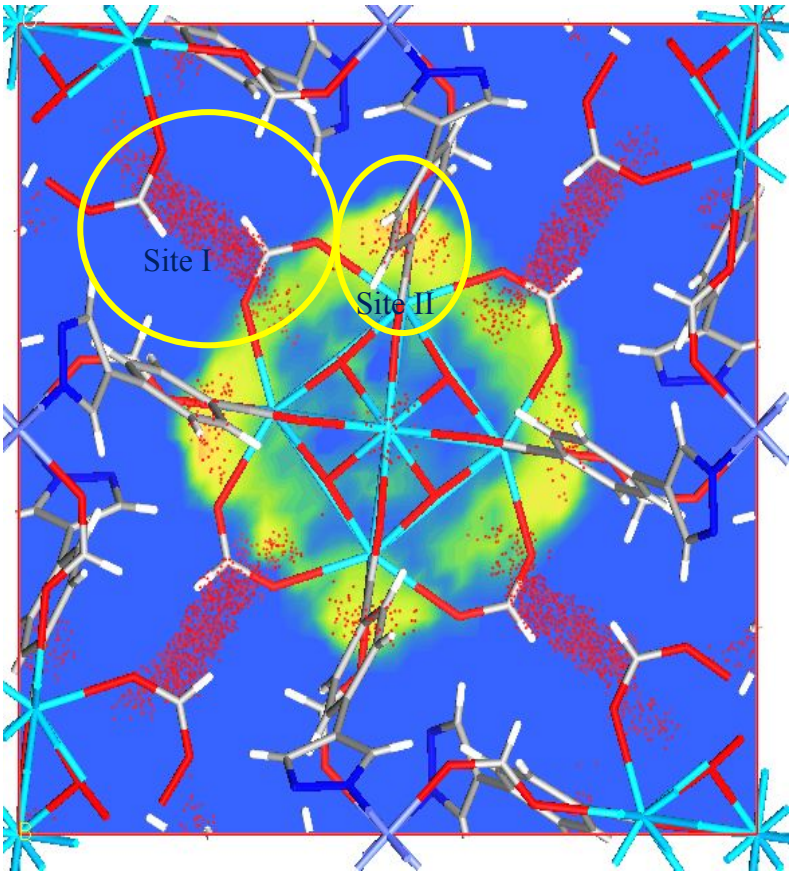

Figure S14. View of the adsorption density of SO_2 in MOF-Th-Co-67 in site I and II.

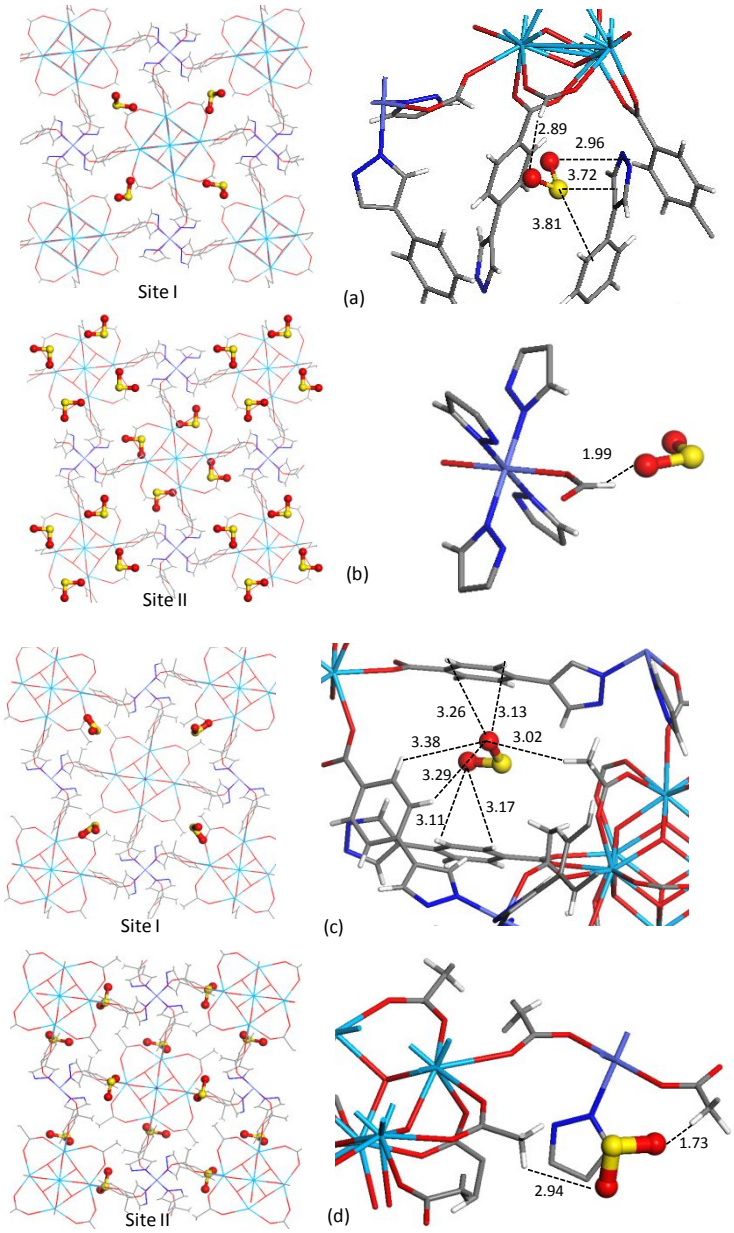

Figure S15. (a) and (b) View of sites I and II in **MOF-Th-Co-66**. (c) and (d) View of sites I and II in **MOF-Th-Co-67**.

Table S1. Crystal data and structure refinement for **MOF-Th-Co-66**.

Temperature	296 (2) K
Wavelength	0.71073 Å
Crystal system	Tetragonal
Space group	*I4/m*
Unit cell dimensions	a = 18.0016(19)Å
	b = 18.0016(19)Å
	c = 23.092(5) Å
Volume	7483.1(19) $Å^3$
Z	4
Density (calculated)	1.548 Mg/m^3
F(000)	3220
Completeness to theta = 24.804°	99.9%
Goodness-of-fit on F^2	1.071
Final R indices [I>2sigma(I)]	R1 = 0.0322, wR2 =0.1026
R indices (all data)	R1 = 0.0359, wR2 =0.1042
CCDC number	2131573

$aR_1 = \Sigma||F_o| - |F_c|| / \Sigma|F_o|$ (based on reflections with $Fo^2 > 2\sigma F^2$); $wR_2 = \{\Sigma[\omega(Fo^2 - Fc^2)^2]/\Sigma[\omega(Fo^2)^2]\}^{1/2}$; $w = 1/[\sigma^2 F_o^2 + (0.095P)^2]$; $P = [\max(Fo^2, 0) + 2Fc^2]/3$ (also with $Fo^2 > 2\sigma F^2$).

Table S2. Crystal data and structure refinement for **MOF-Th-Co-67**.

Temperature	296 (2) K
Wavelength	0.71073 Å
Crystal system	Tetragonal
Space group	*I4/m*
Unit cell dimensions	a = 17.9055(18)Å
	b = 17.9055(18)Å
	c = 22.910(5) Å
Volume	7345(2) $Å^3$
Z	4
Density (calculated)	1.626 Mg/m^3
F(000)	3332
Completeness to theta = 24.804°	99.9 %
Goodness-of-fit on F^2	1.089
Final R indices [I>2sigma(I)]	R1 = 0.0325, wR2 = 0.0763
R indices (all data)	R1 = 0.0364, wR2 = 0.0776
CCDC number	2131574

$aR_1 = \Sigma||F_o| - |F_c|| / \Sigma|F_o|$ (based on reflections with $Fo^2 > 2\sigma F^2$); $wR_2 = \{\Sigma[\omega(Fo^2 - Fc^2)^2]/\Sigma[\omega(Fo^2)^2]\}^{1/2}$; $w = 1/[\sigma^2 F_o^2 + (0.095P)^2]$; $P = [\max(Fo^2, 0) + 2Fc^2]/3$ (also with $Fo^2 > 2\sigma F^2$).

Table S3. Dual-site Langmuir parameter fits for SO_2 and CO_2 in MOF-Th-Co-66.

	Site A			Site B		
	$q_{A,sat}$ mol kg^{-1}	b_A Pa^{-1}	E_A kJ mol^{-1}	$q_{B,sat}$ mol kg^{-1}	b_B Pa^{-1}	E_B kJ mol^{-1}
SO_2	5.3	1.112E-09	28	4	4.833E-12	28.4
CO_2	3.9	3.315E-10	24			

Table S4. Dual-site Langmuir parameter fits for SO_2 and CO_2 in MOF-Th-Co-67.

	Site A			Site B		
	$q_{A,sat}$ mol kg^{-1}	b_A Pa^{-1}	E_A kJ mol^{-1}	$q_{B,sat}$ mol kg^{-1}	b_B Pa^{-1}	E_B kJ mol^{-1}
SO_2	1	3.390E-05	9.1	7	1.598E-11	36
CO_2	7.2	6.597E-10	20.7			